ABSTRACT

Title of thesis: Terahertz Detection and Mixing Using Two-Dimensional Materials

Edward S. Leong, Master of Science, 2016

Thesis directed by: Professor Thomas E. Murphy
Institute for Research in Electronics & Applied Physics
Department of Electrical & Computer Engineering

The discovery of graphene in 2004 and the rise of the two-dimensional materials provide an excellent platform for developing optoelectronics for terahertz (THz) detection and mixing. For graphene and black phosphorus, their high carrier mobility, attractive electrical and thermal properties show promises for tunable terahertz technology.

In the first part of the thesis, we discuss the THz photoresponse of black phosphorus (BP). The rediscovery of BP as a two-dimensional material in 2014 has drawn attention to its near and mid-infrared application. Here, we present an ultrafast THz detector based on black phosphorus with high efficiency at room temperature. The detector has a noise equivalent power of 130 $\mu\mathrm{W}/\sqrt{\mathrm{Hz}}$ at 2.5 THz, and an ultrafast photoresponse of about 20 ps was observed. Two detection mechanisms were observed: a strong photothermoelectric effect and a weak bolometric effect. The high carrier mobility allows BP to absorb THz radiation through free-carrier absorption, even thought the photon energy (10 meV) is far below the band gap (300 meV) of the material. The intrinsic responsivity of BP is also estimated via a Joule-heating

experiment and using a free-carrier model.

In the second part of the thesis, we discuss down frequency mixing and the fabrication process of a graphene FET mixer. Graphene exhibits a significant change in conductivity when the Fermi energy is altered by applying a gate voltage. Near the Dirac point, graphene field effect transistors (FETs) show a strongly nonlinear response (i.e. a nonlinear change in resistivity with applied gate voltage) that can be exploited to provide efficient rectification and mixing of THz signals. Although rectification in graphene field-effect transistors has been demonstrated, heterodyne mixing in the THz band has not been explored. We examine a THz graphene mixer using an antenna-coupled graphene FET configuration. We will discuss the antenna and graphene device design optimized for heterodyne mixing at 0.35 THz. In addition, fabrication and preliminary measurements of a microwave frequency prototype will be presented to demonstrate the principle of the operation.

Terahertz Detection and Mixing Using Two-Dimensional Materials

by

Edward S. Leong

Thesis submitted to the Faculty of the Graduate School of the
University of Maryland, College Park in partial fulfillment
of the requirements for the degree of
Master of Science
2016

Advisory Committee:
Professor Thomas E. Murphy, Chair/Advisor
Professor Mario Dagenais
Professor Martin Peckerar

© Copyright by
Edward S. Leong
2016

Table of Contents

List of Figures iv

1 Introduction 1
- 1.1 Characteristics and Applications in THz Region 2
- 1.2 Advances in THz Technology 3
- 1.3 Two-Dimensional Materials 4
  - 1.3.1 Graphene 4
  - 1.3.2 Black Phosphorus 5
- 1.4 Graphene Field-Effect Transistor 6
- 1.5 Heterodyne Mixing 9
- 1.6 Photo-thermoelectric Effect 9

2 Black Phosphorus Terahertz Detector 12
- 2.1 Overview 12
- 2.2 Methods 13
  - 2.2.1 Device Fabrication 13
  - 2.2.2 Experimental Setup 14
    - 2.2.2.1 DC Characterization 14
    - 2.2.2.2 Optical Characterization 15
    - 2.2.2.3 Terahertz System 16
    - 2.2.2.4 Time Resolved Measurement 17
    - 2.2.2.5 2ω Measurement 17
- 2.3 Results and Analysis 19
  - 2.3.1 DC Characterization 19
  - 2.3.2 Optical Characterization 20
  - 2.3.3 Angle Dependence Measurement 20
  - 2.3.4 Gate and Bias Dependence Measurement 23
  - 2.3.5 Power Dependence 24
  - 2.3.6 Spatially Resolved Measurement 25
  - 2.3.7 2ω measurement 25
  - 2.3.8 Free-carrier Model 27
  - 2.3.9 Time-resolved Measurement 28
- 2.4 Discussion and Future Work 29

3 Graphene FET Mixer 32
3.1 Overview 32
3.2 Methods 32
3.2.1 Design of The Graphene Mixer 32
3.2.2 Device Fabrication 34
3.2.3 Experimental Setup 35
3.2.3.1 DC Characterization 35
3.2.3.2 Frequency Mixing Measurement 36
3.2.3.3 Data Acquisition 37
3.3 Results and Analysis 38
3.3.1 DC Characterization 38
3.3.2 Frequency Dependence 39
3.3.3 Power Dependence 40
3.3.4 Gate and Bias Dependence 41
3.4 Discussion and Future Work 44

4 Conclusion 47

Bibliography 49

List of Figures

1.1 Terahertz region in the electromagnetic spectrum. Reprinted from ref. [1]. 2
1.2 Atomic structure of monolayer black phosphorus. Reprinted from ref. [2], with permission from Nature Publishing Group, Copyright 2015. 6
1.3 Cross section of a field-effect transistor 7
1.4 Ambipolar characteristic of a graphene field-effect transistor. Reprinted from ref. [3], with permission from Nature Publishing Group, Copyright 2007.) 8
1.5 Schematic diagram for down frequency mixing 10
1.6 Photo-thermoelectric effect in schematic diagram (a)without asymmetry in the device (b) with asymemetry in the device. 11

2.1 (a) Gating curves of the BP FET at different temperatures. V_{Gate} was applied to back gate. (b) Optical micrograph of the antenna with the black phosphorus flake in the center 14
2.2 Setup for the DC characterization 15
2.3 Setup for generating ultrafast THz pulse 18
2.4 Polarization dependence of NIR photocurrent measurement 21
2.5 Polarization dependence of the photovoltage measured at 1.55 um (red) and 120 um (black). 22
2.6 THz photovoltage as a function of the (a) gate voltage (V_{SD}=0) and the (b)source-drain bias(V_G=0). The insert in (b) shows the linerity of the measured photoresponse(V_{SD}=0, V_G=0). (c)Spatially resolved photovoltage measurement measured at 1.56 μm 24
2.7 (a) Schematic of the 2ω measurement setup to determine the intrinsic responsivity. (b) Second harmonic generated by the photothermoelectric effect in the black phosphorus flake. 26
2.8 Time-resolved measurement of the photovoltage signal obtained at a frequency of 0.5 THz and a pulse duration of about 1 ps. 30

3.1 Optical micrograph of the graphene mixer with the graphene on the center 33

3.2 Device fabrication process for the graphene mixer in cross section and the corresponding micrographs. (a) Graphene patterning (b) Metal deposition for drain and source contacts (c) Al_2O_3 deposition by ALD (d) Gate metal deposition (e) Al_2O_3 etch for contact area 35
3.3 (a) Setup for the RF mixing measurement 37
3.4 DC gating curve of the graphene FET 39
3.5 (a) Frequency mixing measurement of the graphene mixer. The IF output power is measured with RF and LO frequencies from 16-40 GHz 40
3.6 Output spectrum of the IF at 956 MHz. The corresponding RF and LO frequency are 30.956 GHz and 30 GHz. 42
3.7 (a) Frequency mixing measurement for the graphene mixer as a function of input power. The RF power ranges from -20dbm-10dbm with 20dBm LO power. The measurement is done at the frequency of 30 GHz 42
3.8 Frequency mixing measurement for the graphene mixer as a function of input power. The RF power ranges from -20 - 10 dbm with 20 dBm LO power. The measurement is done at the frequency of 30 GHz 44

Chapter 1: Introduction

The "terahertz (THz) gap" is one of the least exploited regions in the electromagnetic spectrum. It lies between microwaves and the optical frequencies, and loosely defined as the frequency range from 0.1 THz to 10 THz. While the lower frequencies are accessible by conventional electronics, the electronics are limited by their speed when it reaches to the THz frequencies. On the other side, traditional methods in classical optics don't apply well on the THz band. The lack of devices and apparatuses was the main challenge to make use of the THz radiation. The THz region was first explored by H. Rubens and his colleagues in the late 1800s [4]. As technology advances, THz waves have been used as a tool to explore nature. For example, THz spectroscopy has become a useful tool to study condensed matter physics [5]. Astrophysicists have also been observing the signatures from the big bang in the THz band [6]. THz technology not only allows us to explore the nature of our world; it also has wide range of applications in medical imaging, security, and ultrafast wireless communication [7–9].

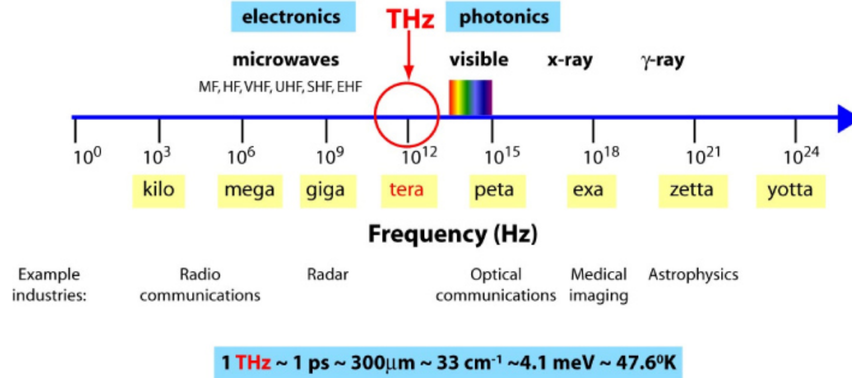

Figure 1.1: Terahertz region in the electromagnetic spectrum. Reprinted from ref. [1].

1.1 Characteristics and Applications in THz Region

Being in between microwaves and infrared, THz radiation shares some properties from both regimes. Many non-conducting materials are transparent to THz radiation, and THz wave is non-ionizing. A wide field of interesting physics, e.g. phase transitions, molecular transitions, or excitation of excitons in semiconductors take place in this field. These properties lead to numerous commercial applications. For examples, THz wave is attractive for medical imaging because it is non-ionizing. Unlike X-rays, THz waves have lower photon energy that generally doesn't damage human tissue. It can therefore be safely used even without protective equipment that is normally used in radiology. Medical applications like screening for skin cancer and imaging teeth has been demonstrated [7, 10–13]. Similar to microwaves, a wide range of non-conducting materials(i.e. clothing, plastic, wood, and paper) are transparent to THz radiation. While water and metal are not transparent in this region, THz waves have great potential for security screening, and provide a quick way for non-invasive body scans, and rapid identification of concealed weapons [14].

Its security applications can extend to detecting explosives and toxic gases [6, 9]. Many molecules have unique spectral signatures in THz absorption. These signatures can be used to determine the presence of explosives and various toxic gases. Another important application is in high-speed wireless communication. THz waves can provide high speed communication links with large data rate [8, 15], becasue of the higher carrier frequency. Therefore, THz technology can extend the bandwidth of wireless communication and carry more mobile users.

1.2 Advances in THz Technology

The "THz gap" has been gradually filled as the development of optoelectronic and semiconductor technology advances. As mentioned above, the main obstacle to use the THz band has been the lack of devices and sources that operate at those frequencies. While the frequency of THz is too high for conventional electronics, the photon energy of THz radiation is smaller than the band gap of semiconductors. For this reason, THz waves are difficult to manipulate and control by traditional electronics and photonics. In the past decades, THz technology has been advanced by the tremendous effort of researchers. Many THz devices and systems have been invented to fill the gap. For example, Ti:sapphire-based lasers has been used to drive THz emitters based on frequency downconversion and optical rectification to generate THz pulses [16, 17]. Also in 1994, quantum cascade lasers were first demonstrated by Faist and Capasso, and it can generate power in the mW range at frequencies as low as 5 THz. Other examples of THz sources are free electron laser

(FEL) and backward wave oscillators (BWO), which have been developed to generate high power THz radiation [18–22]. For sensing THz radiation, several types of detector were developed as well, each with their own advantages and disadvantages. For example, the hot electron bolometer (HEB) offers extremely high sensitivity and fast detection. It has been shown that HEB can have the high sensitivity for THz detection with a time constant on the order of μs [23]. However, most sensitive bolometers require cryogenic cooling to bring down the temperature below 4 K. On the other side, Schottky-barrier diode detectors have the advantage of fast detection in ns range and room temperature operation. The drawback is its sensitivity diminishes at higher frequencies. The Golay cell is notable for its high sensitivity with using thermal detection. However, the speed of the detector is limited to ms order. Pyroelectric detection is another example that uses thermal detection. It is commercially available and very sensitive to THz radiation, but it only offers detection speed for several kHz.

1.3 Two-Dimensional Materials

1.3.1 Graphene

Graphene is a monolayer of carbon atoms arranged in the form of a 2D honeycomb lattice. Its electrical and optical properties make it an attractive material for THz applications. Charge carriers in graphene behave like massless Dirac fermions [24]. Exceptionally high carrier mobility has been achieved in graphene, and mobility of 230,000 $cm^2/(V\cdot s)$ was measured on suspended graphene at 5 K [25].

Monolayer graphene is also a zero-band gap semimetal. The valence band and conduction band meet at the Dirac point. When the Fermi energy is at this point, the conductivity of the graphene sheet reaches its minimum. In theory, graphene has a linear energy dispersion relation in the momentum space, and it allows broadband absorption [26]. Saturable absorption has been observed in graphene because of Pauli blocking. Under illumination at high intensity, carriers in graphene are excited and fill up the higher energy states. Before the carriers relax to lower energy states, the absorption is partially blocked as some of the excited states are already populated. Saturable absorption can be used for mode-locking, and a mode-locked ultrafast laser on graphene has been demonstrated based on this effect [27]. Graphene also has excellent compatibility with a variety of substrates and is stable in ambient conditions [28]. It can be transferred to wide variety of substrates and held by van der Waals force. This allows graphene to be integrated with different optical and electrical devices without significantly changing its properties [29].

1.3.2 Black Phosphorus

Black phosphorus (BP) is one of the most stable allotropes of phosphorus. Bulk crystal of BP is comprised of a stack of individual atomic layers held together by van der Waals forces. Similar to graphene, it can be mechanically exfoliated to monolayer or few-layers. Thin layers of black phosphorus retain its characteristic as semiconductor. It possesses direct band gap, and the band gap energy is determined by the number of the layers in the stack. For monolayer BP, the band gap energy is

about 2 eV, and it reduces to the band gap energy of about 0.3 eV in the bulk crystal as the number of layers increases [30]. The direct band gap and variable band gap energy make it favorable for optoelectronics [31]. In contrast to graphene, BP FET can be almost turned-off due to the existence of a band gap. A high on-off ratio of 10^5 can be achieved in room temperature for BP FET devices [32]. BP is also an anisotropic optical and electronic material due to it puckered atomic structure. Monolayer of BP has 2 distinct in-plane directions: the zigzag and armchair direction as shown in Figure 1.2. High mobility of about 1000 $\mathrm{cm}^2/(\mathrm{V}\cdot\mathrm{s})$ was found on BP along the armchair direction [32]. The optical transmission is also anisotropic, where light polarized along the zigzag direction has highest transmission.

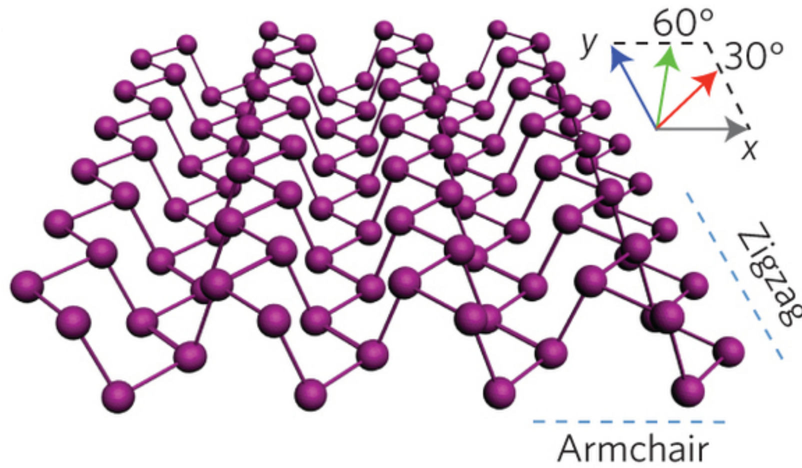

Figure 1.2: Atomic structure of monolayer black phosphorus. Reprinted from ref. [2], with permission from Nature Publishing Group, Copyright 2015.

1.4 Graphene Field-Effect Transistor

A field-effect transistor (FET) is a three terminal device in which the conductivity between the so called source and drain terminals can be controlled via a gate

voltage that is applied to the gate and source terminal. As shown in Figure 1.3, conventional FET has the capacitive gate in between the source and drain terminal, and the gate is isolated from the substrate by an oxide or other insulating layer. When a gate voltage is applied, the gate acts like a capacitor, and charge carriers are induced on the substrate in between the source and drain. These charge carriers form a conductive path between the source and drain, referred to as the channel. When bias voltage is applied to the source-drain, the channel carries a current that can be modulated by the applied gate voltage. Conventional FETs employ classic

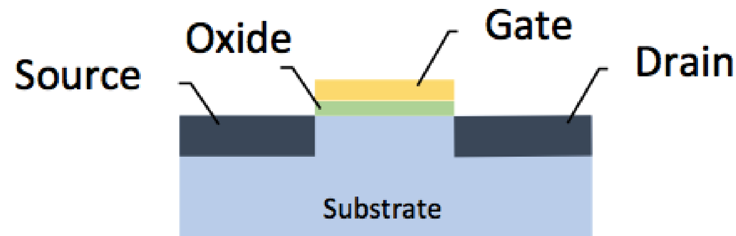

Figure 1.3: Cross section of a field-effect transistor

semiconductors like Si or GaAs. Graphene can replace these classical materials as active channel materials, leading to a new type of FET, the so called graphene FET (GFET). The Fermi energy of the graphene can be controlled by the electric field from the applied gate voltage. Since the conductivity of graphene depends on the Fermi level, the conductance of the graphene can be tuned by the gate voltage. Figure 1.4 shows the carrier transport characteristic of an ideal graphene FET. When the gate voltage is positive, the conduction band is populated by electrons and the Fermi level is in the conduction band. On the other hand, the graphene become p-type when the Fermi level lies in the valence band and the transport is governed

by holes. The conductivity of the graphene reach its minimum when the Fermi level approaches the Dirac point, where the conduction and valence band meet [24]. As shown on Figure 1.4, graphene FETs have the ambipolar transport characteristics. The type of charge carriers are controlled by the gate voltage, and the drain current exhibits symmetry about the Dirac point. The speed of the FET limited by the carrier mobility in the channel. Graphene can have high mobility of over 100,000 $cm^2/(V{\cdot}s)$ at room temperature [33] while Si has electron mobility of about 1,400 $cm^2/(V{\cdot}s)$, and therefore, Graphene FETs have great potential for high frequency applications.

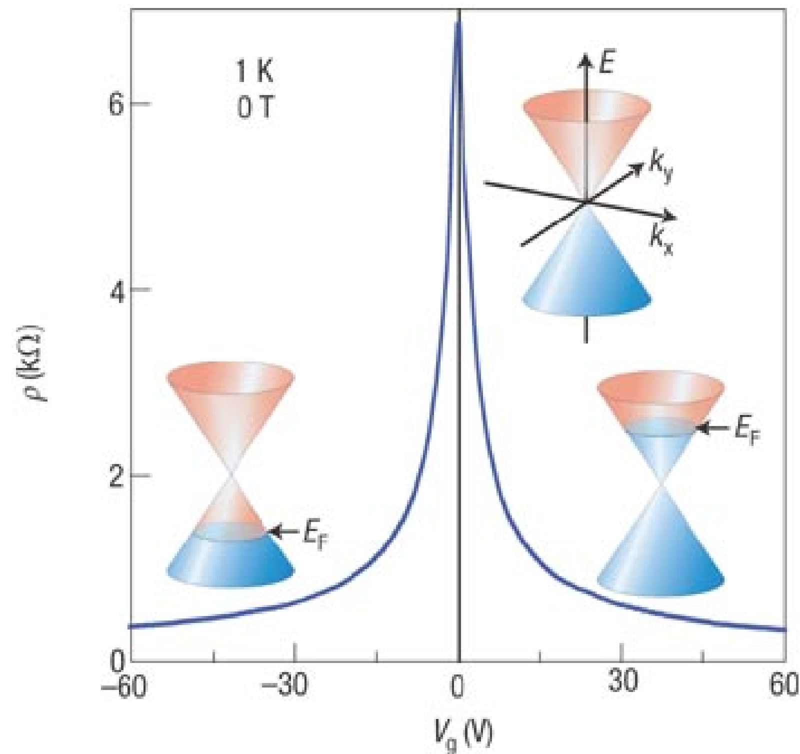

Figure 1.4: Ambipolar characteristic of a graphene field-effect transistor. Reprinted from ref. [3], with permission from Nature Publishing Group, Copyright 2007.)

1.5 Heterodyne Mixing

Heterodyne mixing involves two input signals at different frequencies. The mixing process combines the two signals and generates two output signals at the sum and difference frequency of the two inputs. Provided two AC signals have frequencies at f_1 and f_2, heterodyne mixing combines two in a nonlinear element, and generates output signals at frequencies $|f_1 + f_2|$ and $|f_1 - f_2|$. Heterodyne mixing is a commonly used technique to up-convert or down-convert the frequency of the signal to the desire range for signal processing. For downconversion in radio frequency (RF), a small RF signal mixes with a strong local oscillator (LO), to produce an output signal at a lower intermediate frequency (IF) $|f_1 - f_2|$ while the high sum frequency $|f_1 + f_2|$ is filtered out. The nonlinear element that performs frequency mixing is called a mixer. This component can be a Schottky diode, transistor, superconductor-insulator-superconductor (SIS) mixer etc. While the frequency range of most conventional mixers is limited to the GHz range, SIS mixers can be operated at THz frequencies, but require cooling to liquid helium temperature. In the third chapter of this thesis we will discuss mixers that are based on GFETs, which potentially allow efficient mixing in the THz range at room temperature.

1.6 Photo-thermoelectric Effect

Whenever electromagnetic radiation is absorbed by a material, the temperature of the carriers increases. The hot carriers will diffuse to the region that has

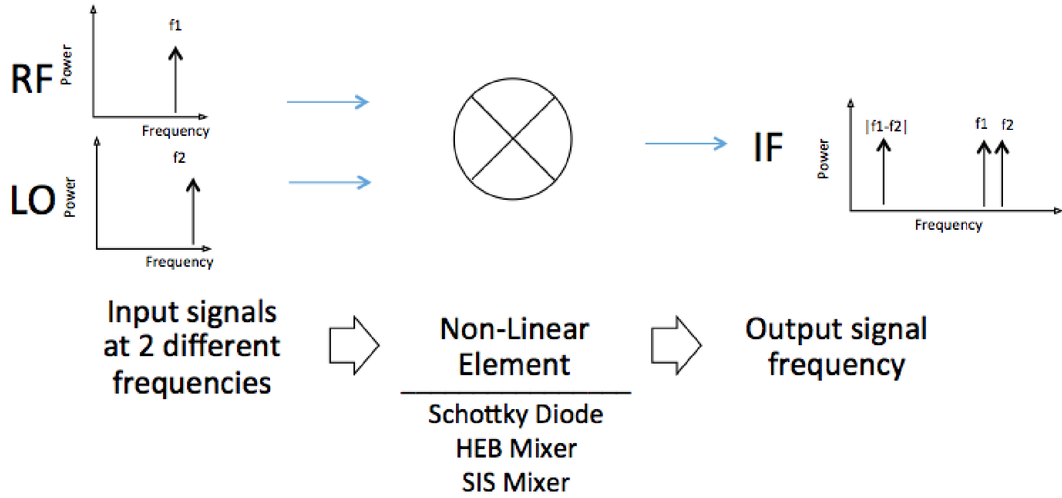

Figure 1.5: Schematic diagram for down frequency mixing

lower temperature as shown in Figure 1.6. On a symmetric device that has identical metal contacts on both sides, the hot carriers will diffuse evenly in both directions from the center to the metal contacts. In this case, the net current will be zero because the current flow in both directions will cancel one another. On the other hand, asymmetry can be introduced in the device by local gating [34, 35], local excitation [36] , or by using dissimilar metal contacts [37]. In these cases, there can exist a temperature gradient across the device, that will drive the hot carriers to a particular direction instead of letting them diffuse evenly in both directions. Even without electrical bias or voltage, a net current can be produced by the absorbed radiation because of the asymmetry in the temperature profile. The direction of the induced current will follow the temperature gradient.

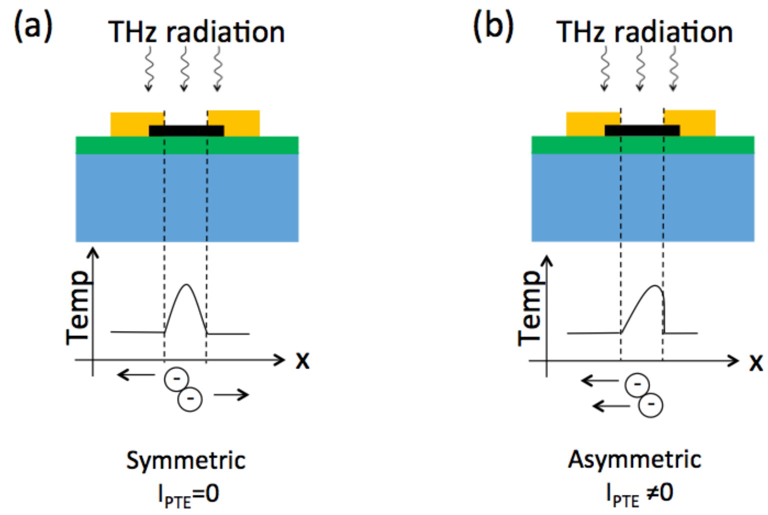

Figure 1.6: Photo-thermoelectric effect in schematic diagram (a)without asymmetry in the device (b) with asymemetry in the device.

Chapter 2: Black Phosphorus Terahertz Detector

2.1 Overview

A BP THz detector was fabricated to study the THz response of BP. As shown in Figure 2.1 (b), a logarithmic-periodic antenna was attached on the BP to more efficiently couple the THz radiation from free space. The antenna was also used to provide electrical contact to the BP flake. Under the BP, the lightly doped Si substrate was isolated from the BP by a layer of SiO_2. The Si substrate was used a capacitive gate, and the electrical contacts from the antenna served as source and drain contacts. The back gate under the SiO_2, together with the source and drain contacts from the antenna form a FET structure with the BP. Similar to graphene FETs, this BP FET has a few layers of BP that serves as the conductive channel. This allows the carrier density of the BP to be controlled by the capacitive gate voltage applied to the back gate.

2.2 Methods

2.2.1 Device Fabrication

The antenna-coupled BP THz detector was fabricated by using a mechanically exfoliated BP flake and contact photolithography. The fabrication process begins with a Si/SiO_2 substrate with a 300 nm thick SiO_2 thermal oxide on top. The Si substrate is lightly doped and has the resistivity of 250 $\Omega \cdot$ cm, which allows a voltage to be applied to substrate for the back gate, as described in section 2.1. A BP thin flake is then mechanically exfoliated on the top of the oxide layer from a bulk crystal. Thin layers of BP degrade in ambient atmosphere because of the oxygen and moisture [38, 39]. To minimize the exposure to ambient air, photoresist was immediately spun on the top of the BP as a protective layer. After that, we used a mask aligner to align the antenna pattern to the BP flake. The photoresist was exposed to UV light, to form an antenna pattern attached to the BP. The antenna on the BP also served as the source and drain contacts as shown on Figure 2.1. 10 nm/100 nm of Cr/Au were deposited for the ohmic contacts with the antenna, followed by the metal lift-off in acetone. A 100 nm thick layer of Al_2O_3 was subsequently deposited on the top by atomic layer deposition. The Al_2O_3 layer covers the BP film and isolates it permanently from the atmosphere to prevent degradation [39]. The Al_2O_3 layer is then selectively removed at the location of the source-drain contacts by wet chemical etching, to allow electrical contact.

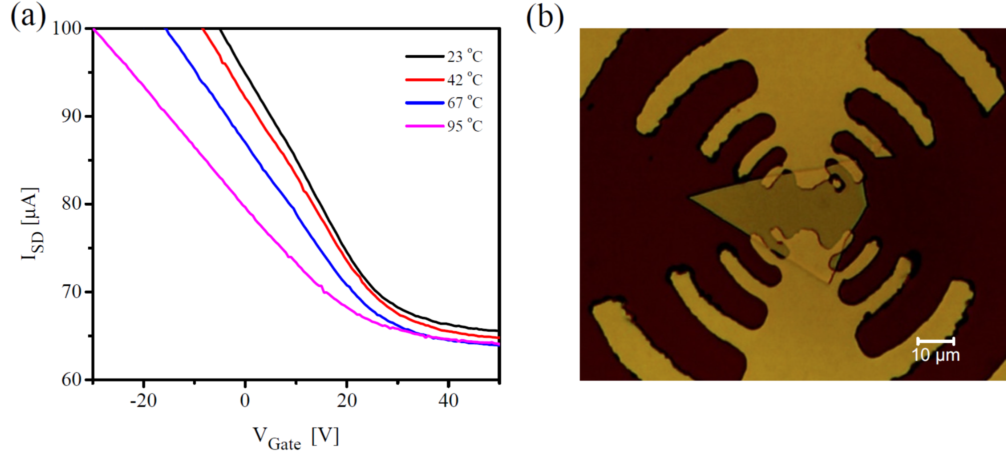

Figure 2.1: (a) Gating curves of the BP FET at different temperatures. V_{Gate} was applied to back gate. (b) Optical micrograph of the antenna with the black phosphorus flake in the center

2.2.2 Experimental Setup

2.2.2.1 DC Characterization

The DC transport characteristics of the BP FET were investigated by measuring its DC gating response. Similar to graphene, the Fermi energy of the BP is tunable by changing the applied gate voltage. Therefore, the conductance of the BP can be measured as a function of the gate voltage. Figure 2.2 shows a diagram of the DC measurement. A pair of programmable DC sources (Keithley 2400) were connected to the detector via needle probes. One of the sources controlled the gate voltage of the BP FET while monitoring the leakage current. The other set the source-drain bias and measured the drain current from the device simultaneously. The sourcemeters were programed by Matlab to sweep the gate voltage and take both measurements simultaneously. The source-drain bias was kept at 0.1 V, and the drain current was kept below 100 μA to avoid Joule heating. The gate voltage

was swept from -50 V to 50 V, and the drain current was recorded to obtain the gating curve of the BP FET. To understand the temperature dependence, the BP device was placed on top of a hotplate to set different temperatures for the measurement. The measurement of the gating curve was repeated at various temperatures to observe the effect on the conductivity of BP.

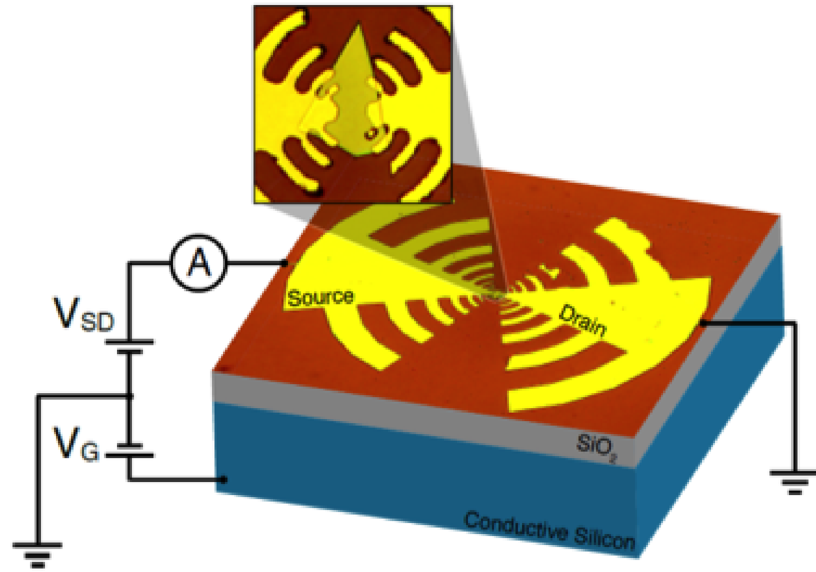

Figure 2.2: Setup for the DC characterization

2.2.2.2 Optical Characterization

A near-infrared (NIR) laser system was used to characterize the material properties of BP in order to understand the THz response of a BP detector. The anisotropy of BP contributes to its strong dependence on the polarization of NIR illumination due to the corrugation in the crystal lattice [40]. The spatially resolved measurement in the NIR also helps to elucidate the nature of the photodetection mechanism in the BP detector. Thus, we measured the NIR response of the BP

detector and used it as tool to understand some of the observed behaviors at THz frequencies. The setup of the NIR system is described as the following: A fiber optic laser with 1.5 μm wavelength was used as the source of NIR illumination. The laser was linearly polarized and a half wave plate was inserted in the beam path to control the state of polarization. The NIR beam was also mechanically chopped at a frequency of 550 Hz, which allowed us to use a lock-in amplifier to read out the signal. We further focused the NIR beam with an aspherical lens to a spot size of about 3 μm in diameter. The BP detector was mounted on a three-axis translation stage for the spatial adjustment to perform the spatially resolved measurement under NIR illumination. A lock-in amplifier was connected to the BP detector through a transimpedance amplifier. The NIR response of the BP detector is measured by the lock-in amplifier.

2.2.2.3 Terahertz System

The THz response of the BP detector was measured as a function of the incident light polarization, incident power, gate voltage, and source-drain bias. We used a CO_2 pumped methanol laser at a frequency of 2.5 THz for the source of radiation. The maximum power of the THz beam was 6 mW, and the beam was mechanically chopped at 50 Hz. We directed the beam to pass through a half wave plate to allow us control the polarization of the THz radiation. The beam was focused onto the BP detector using an off-axis parabolic mirror. The spot size of the focused THz beam was about 200 μm in diameter. The BP detector was mounted

on a three-axis translation stage. It allowed the position scanning in x, y, and z direction to find the optimum position for the measurement. A lock-in amplifier was connected to the BP detector via a transimpedence amplifier, which enabled the lock-in detection with the intensity modulated THz laser beam at a frequency of 50 Hz. Additionally, the back gate of the BP detector was connected to a Keithley sourcemeter to allow the adjustment of the gate voltage, while the transimpedance amplifier provided the source-drain bias of the BP detector.

2.2.2.4 Time Resolved Measurement

Ultrashort THz pulses generated by optical rectification in a $LiNbO_3$ crystal were used to observe the THz photoresponse in the time domain. A LiNbO3 crystal is pumped by laser pulses at 800 nm with duration of about 40 fs at a repetition rate of 1 kHz. This generates an ultrashort THz pulse with duration of about 1 ps [41]. A polymethylpentene (TPX) lens focused the THz radiation onto the BP detector. The scattered 800nm pump light is blocked by a Si window which was placed in front of the BP detector. The signal from the BP device is recorded with a sampling oscilloscope with a bandwidth of 40 GHz at three different pulse energies.

2.2.2.5 2ω Measurement

The intrinsic thermoelectric response of the BP device can be estimated by using the 2ω measurement. The 2ω method is a purely electrical measurement that measures the thermoelectric voltage from the power absorbed via Joule heating.

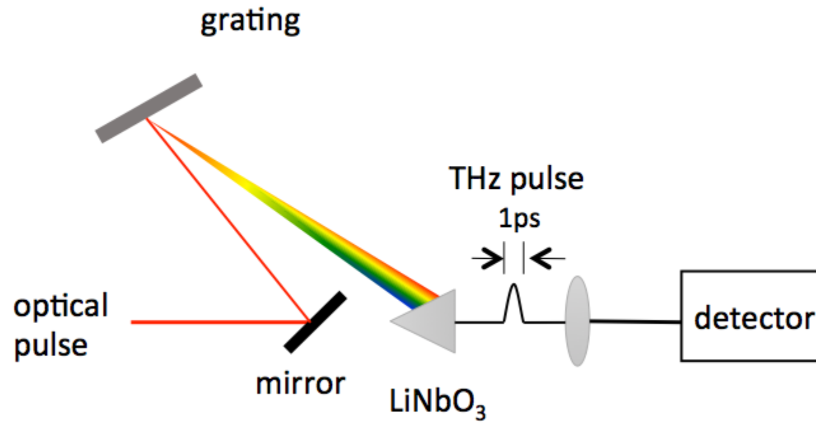

Figure 2.3: Setup for generating ultrafast THz pulse

Measuring the intrinsic thermoelectric responsivity optically can be challenging, because it is difficult to take into the account the coupling efficiency and all the losses in a THz system. The 2ω method provides a simple alternate way to estimate the intrinsic responsivity. The circuit diagram of the setup is shown in Figure 2.7. An AC voltage at 5 kHz was applied to a current-limiting resistor. An AC current, $I_0 \sin(\omega t)$, was applied to the BP. The current limiting resistor is 100 kΩ, which has a much higher resistance than the BP device of about 1 kΩ. The current limiting resistor converts the AC voltage to a stable AC current through the BP device. In parallel to the BP detector, a lock-in amplifier was connected to measure the thermal voltage at a frequency of 2ω generated by Joule heating.

2.3 Results and Analysis

2.3.1 DC Characterization

From the I-V characteristic of the BP FET, we can estimate the carrier mobility of the BP flake. The BP flake is slightly p-doped as shown on the gating curve. Without a gate voltage applied, the majority carriers in the channel are holes. They are primarily responsible for the current transport. In BP, holes have higher mobility comparing to electrons [40]. The field-effect mobility of holes μ_h was calculated by using the relationship [32]

$$\mu_{\mathbf{h}} = \frac{L}{W}\frac{1}{C_g}\frac{dG}{dV_g}\,. \tag{2.1}$$

L/W represents the length to width ratio of the channel. C_g is the capacitance per unit area of the gate. G is the DC conductance of the channel, and V_g is the applied gate voltage. By using the data shown on Figure 2.2 for calculation, we obtained the hole mobility of (870 ± 70) $\mathrm{cm}^2/(\mathrm{Vs})$ at room temperature. The number of layers in the flake contribute to the high conductance of the BP [32], as flake in this device is relatively thick. Also, the conductivity of the BP shows metallic behavior in that the conductivity decreases as the temperature increases. This strong temperature dependence in the conductivity contributes to the bolometric effect, in which an electrical signal is generated from the change of conductivity caused by the temperature change from the absorbed radiation on the material.

2.3.2 Optical Characterization

The puckered honeycomb lattice in black phosphorus leads to the highly asymmetric band structure [40]. Therefore, BP possesses strong in-plane anisotropy. Along the armchair direction of the crystal lattice, the material shows higher carrier mobility, and it has a lower carrier mobility on the zigzag direction [32], which is perpendicular to the armchair direction. After illuminated by NIR radiation, the absorption strongly depends on the polarization because of this in-plane anisotropy. The photoreponse from the NIR excitation can therefore be utilized to determined the crystal orientation of the BP flake [40]. Figure 2.4 shows the photocurrent measurement as a function of the polarization angle of NIR excitation. The photorespone of the BP is at maximum when the polarization of the NIR excitation aligns with the armchair direction of the crystal lattice, where the BP has higher carrier mobility. On the contrary, the photocurrent is minimized when the radiation is polarized along the zigzag direction. In this plot, the photocurrent of the NIR response on the BP is measured in the steps of 10°. The polarization angle of 0° corresponds to the direction along two electrical contacts. The high mobility axis of the BP is identified at an angle of about 20° relative to the direction along the contacts.

2.3.3 Angle Dependence Measurement

The THz absorption in BP has a different mechanism than NIR absorption due to the lower photon energy of the radiation. Therefore, we performed an angle-

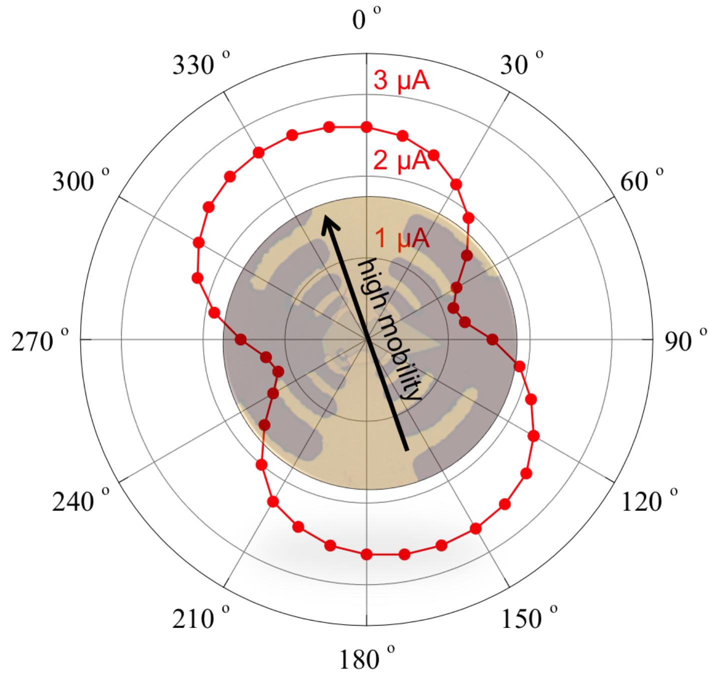

Figure 2.4: Polarization dependence of NIR photocurrent measurement

resolved measurement to study the anisotropy of THz response on BP at 2.5 THz. With using a half-wave plate to rotate the polarization of the THz radiation, the photoresponse was measured with respect to the angle of polarization in steps of 10°. The THz photoabsorption on BP shows substantially stronger anisotropic behavior comparing to the NIR photoresponse. Along the high mobility axis, the THz photoresponse had a strong peak. While the NIR photoabsorption relies on the interband absorption, the THz response is dominated by the free-carrier absorption because the photon energy is much smaller than the band gap. Along the high mobility axis, the high carrier mobility enhances the direct free-carrier absorption, which contributes to the maximum signal of the photorepsonse being observed when the polarization of the incident radiation aligns with the high mobility axis. As the

anisotropy of the mobility stronger than the anisotropy in interband absorption, the photoresponse of the THz radiation has a higher dependence on the polarization angle. A secondary peak is observed when the polarization is at 80°. Along this angle, the incident polarization is aligned with the axis of the antenna that is coupled to the BP. The high resistance of the BP flake limits the coupling efficiency of the antenna, considering the resistance of the BP was about 1 kΩ and the antenna was designed for a 50 Ω load impedance.

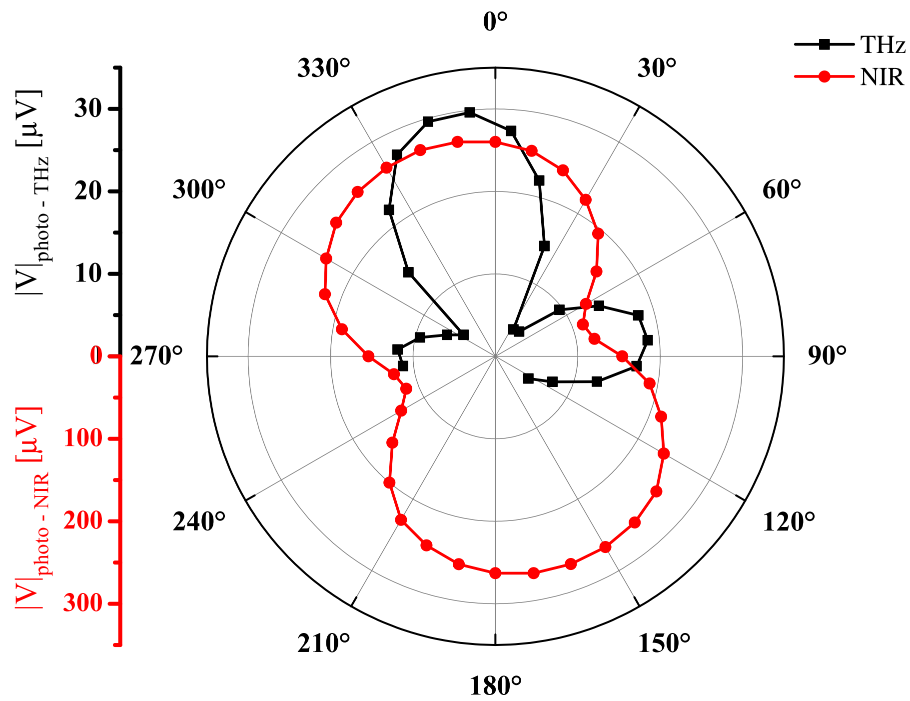

Figure 2.5: Polarization dependence of the photovoltage measured at 1.55 um (red) and 120 um (black).

2.3.4 Gate and Bias Dependence Measurement

To further investigate the origin of the THz photoresponse, we measured the photovoltage as a function of the gate voltage (See Figure 2.6 (a)) as well as a function of the source-drain bias (See Figure 2.6 (b)). In the gate voltage dependence measurement, the maximum signal was observed when the conductivity of the BP was minimized by adjusting the applied gate voltage. Similar behavior was also observed in graphene with the photo-thermoelectric response [37]. In the source-drain bias dependence measurement, we observed a strong signal of 5 μV with zero bias. The contacts appeared to be Ohmic, considering the drain current is linearly proportional to the source-drain bias in the DC measurements. This implies that signal at zero bias does not originate from the photovoltage generated at the Shottky barriers at the contacts. We also observed a weak bolometric response, shown in the bias dependence measurement. Because the THz radiation increases the temperature of the BP flake, the conductivity decreases accordingly. The strong signal mentioned above can't be explained by either a bolometric or photovoltaic effect. The other mechanism that can lead to the photoresponse without bias is photo-thermoelectric effect. The photo-thermoelectric effect is caused by a temperature gradient in the channel within the BP FET. The asymmetry from the gradient drives the charged carriers to the contacts, and produces a photovoltage by the Seebeck effect. This temperature gradient can be formed by local gating [34,35], local excitation [36], or dissimilar metals in the contacts [37].

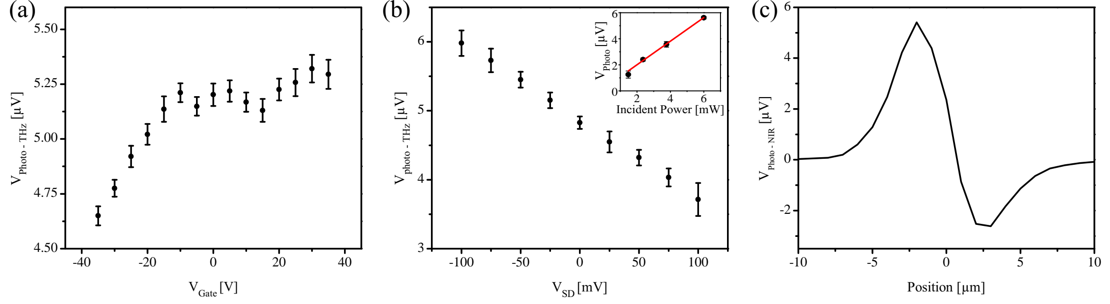

Figure 2.6: THz photovoltage as a function of the (a) gate voltage (V_{SD}=0) and the (b)source-drain bias(V_G=0). The insert in (b) shows the linerity of the measured photoresponse(V_{SD}=0, V_G=0). (c)Spatially resolved photovoltage measurement measured at 1.56 μm

2.3.5 Power Dependence

The THz response of the BP detector as a function of incident radiation power was measured, and the result is shown in the insert of Figure 2.6 (b). The measurements were performed with continuous-wave (CW) laser at 2.5 THz with the incident power ranging from 0 - 6 mW. The results showed that the photoresponse is poportional to the incident power. From that, we estimated the maximum overall responsivity of about 1 mV/W, which is substantially higher than the repsonsivity obtained from similar devices with graphene [42, 43]. Note that the responsivity estimated above does not take into account the losses in the THz system. It is the photorespsonse obtained with power supplied by the THz radiation. The noise equivalent power (NEP) is 130 μW/$\sqrt{\text{Hz}}$ in the measurements. With proper shielding to reduce pickup noise, the noise inherited from the measurement apparatus can be reduced and a NEP of 4.5 μW/$\sqrt{\text{Hz}}$ could be achieved.

2.3.6 Spatially Resolved Measurement

In order to identify the asymmetry causing the charge transfer, a tightly focused near-infrared beam at a wavelength of 1.56 μm was used to investigate the asymmetry of the device by measuring the photovoltage as a function of the spatial position of the near-infrared beam. The result is shown in Figure 2.6 (c). While the space between the contacts is about 10 μm, the focused beam is 1.56 μm diameter which is much smaller than the size of the channel. When the beam was focused on the left side of the contacts, the sign of the photocurrent is positive, and the photocurrent changed sign when the beam was focused on the opposite side. In a symmetrically illuminated device, the photocurrent generated from both contacts would cancel, and sum to a zero net current. On this BP device, a positive net current is generated, because the magnitude of positive peak is stronger than the negative peak. The NIR measurements therefore clearly showed that there was an asymmetry in the channel of the BP device. We believe that in our BP detector, the asymmetry is not caused by the fabrication of the device, but the triangular shape of the BP flake as shown in Figure 2.1 (b).

2.3.7 2ω measurement

The 2ω measurement leverages the Joule heating on the BP, and we can use the response to calculate the intrinsic responsivity. By applying an AC current in the form of $I_0\sin(\omega t)$, the power absorbed by the BP flake can be derived as the

following expression

$$P(t) = \frac{1}{2} R_{\text{Device}} I_0^2 (1 - \cos(2\omega t)) \,. \tag{2.2}$$

The power absorbed by the BP drives a thermal voltage at a frequency of 2ω. With the thermal voltage $V_{2\omega}$ and the calculated absorbed power $P_{2\omega}$, the responsivity of the BP flake can be calculated by

$$\mathbf{R} = \frac{V_{2\omega}}{P_{2\omega}} = \frac{V_{2\omega}}{R_{\text{Device}} I_0^2} \,. \tag{2.3}$$

The result of the 2ω measurement is shown on Figure 2.7 (b), and the estimated intrinsic responsivity is 40 V/W from the measurement. We can then obtain an estimation of the intrinsic responsivity for the absorbed THz power by measuring this thermal voltage at the second harmonic.

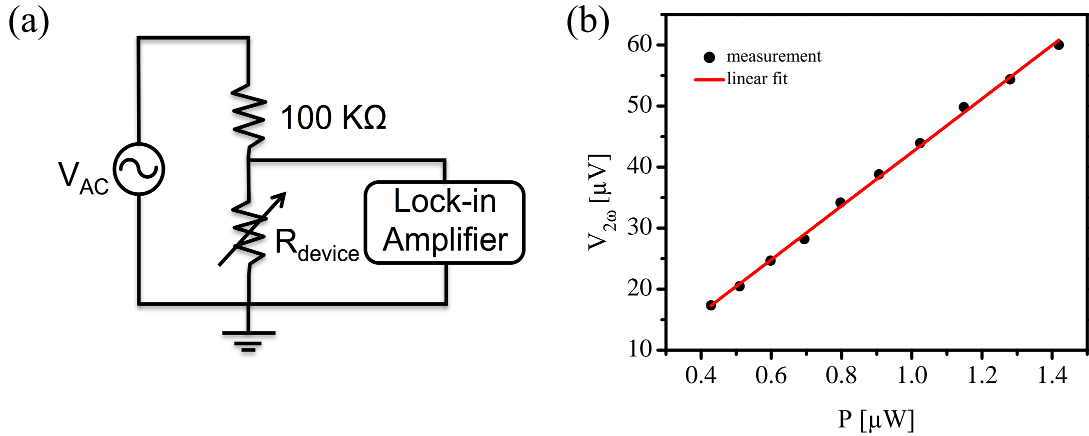

Figure 2.7: (a) Schematic of the 2ω measurement setup to determine the intrinsic responsivity. (b) Second harmonic generated by the photothermoelectric effect in the black phosphorus flake.

2.3.8 Free-carrier Model

The photoresponse of BP THz detector can be estimated by using the free-carrier model with the combination of the intrinsic responsivity from the 2ω measurement. We assumed the free-carrier absorption can be calculated via Drude model. Taking the optical conductivity from the free-carrier model

$$\sigma(\omega) = \frac{\sigma_{\mathrm{DC}}}{1 + \mathrm{i}\omega\tau}\,, \tag{2.4}$$

the reflectivity of the BP film at normal incidence can be estimated with the expression

$$r = \frac{\epsilon_0 c\sqrt{\epsilon_{\mathrm{Si}} - \epsilon_{\mathrm{air}}} + \sigma(\omega)}{\epsilon_0 c\sqrt{\epsilon_{\mathrm{Si}} + \epsilon_{\mathrm{air}}} + \sigma(\omega)}\,. \tag{2.5}$$

This gives a power reflectance of:

$$R \approx |r|^2\,. \tag{2.6}$$

and the transmission can also be calculated with

$$T \approx 1 + |r|^2\sqrt{\epsilon_{\mathrm{Si}} - \epsilon_{\mathrm{air}}}\,. \tag{2.7}$$

Therefore, the free-carrier absorption can be found with the relation

$$\alpha = 1 - R - T\,. \tag{2.8}$$

The σ_{DC} from the equations above is the DC conductivity obtained by the DC characterization. $\epsilon_{\text{ Si}}$ and $\epsilon_{\text{ air}}$ are the relative permittivity of the Si substrate and air respectively. The momentum scattering time τ is the only fit parameter in this calculation. We used the value τ=200 fs for fitting with our experiment data, which is consistent with theoretical expectations [44]. From this we calculated the absorption coefficient α is to be about 0.7 %.

The absorbed power is related to the device geometry and the spot size of the THz beam as described in the expression below.

$$P_{\text{abs}} = \alpha P_{\text{THz}} \frac{A_{\text{Dev}}}{A_{\text{Spot}}} \tag{2.9}$$

And a estimation of absorbed THz power is obtained as P_{abs}=0.13 μW. By using the absorbed power and the intrinsic responsivity calculated above, the photovoltage from the THz response is 5.2 μV from the calculation, which is in good agreement with the THz measurement. In this estimate, we ignore the antenna, under the assumption that the load (BP) is not well matched to the antenna. Thus, A_{Dev} represents simply the geometric area of the BP flake.

2.3.9 Time-resolved Measurement

The result of the time-resolved measurement is shown in Figure 2.8, which shows the ultrafast response from the detector. Our BP detector features a response time of about 30 ps, which is demonstrated by the positive short peak of the signal. The fast response is followed by a ringing with a duration of about 200 ps, possibly

caused by the wiring in the setup. Measurements were also carried out with pulse energy of 100 nJ, 43 nJ, and 25 nJ. While the highest pulse energy is 100 nJ, we used a Si wafer to attenuate the energy of the pulse. The result of the peak of photovotage as a function of the pulse energy is displayed on the inset of Figure 2.8. The photovoltage from the THz response is directly proportional to the pulse energy. The delay present in the lower pulse power are also shown on the plot, which is caused by the transit time through the Si wafers. The response time of a BP detector in near-infrared range is limited by the carrier life time of about 1 ns [45, 46]. With THz radiation, the response is much shorter because no additional carriers are excited.

2.4 Discussion and Future Work

The photothermoelectric effect in the BP detector and the antenna impedance matching can be optimized to substantially improve the performance of the BP device. For better impedance matching for the antenna, the geometry of the channel in the center of the device can be optimized to match the 50 Ω radiation resistance of the antenna. For example, decreasing the channel length to 1 μm and increasing the width to 20 μm would change the resistance of the channel to about 50 Ω. That will match the impedance of the antenna and reduce the loss. Alternatively, using different kind of the shape or type of the antenna can accommodate the impedance mismatch. For the enhancement of the photo-thermoelectric effect, one of the options is using dissimilar metals on the two different contacts on the BP. For

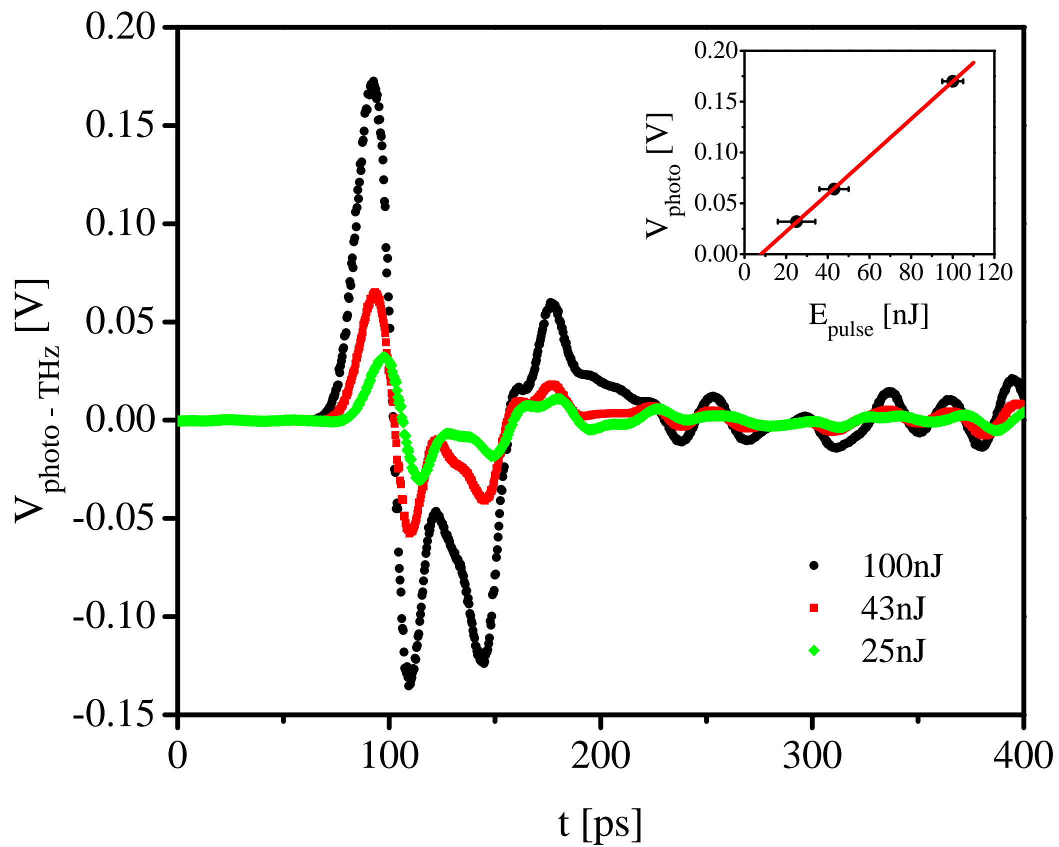

Figure 2.8: Time-resolved measurement of the photovoltage signal obtained at a frequency of 0.5 THz and a pulse duration of about 1 ps.

instance, Au and Cr have a different work function that leads to a different Fermi energy pining in the BP flake at the contacts. Therefore, an asymmetric Fermi energy profile is created [37]. This asymmetry will increase the driving force on the carriers and lead to a higher responsivity on the BP device. Additionally, aligning the high mobility axis of BP flake with the peak of antenna radiation pattern would lead to a stronger THz response as well. Therefore, a more efficient BP THz detector with ultrafast response can be achieved by optimizing the antenna design, contacts, and the geometry of the device.

Chapter 3: Graphene FET Mixer

3.1 Overview

When the Fermi energy of graphene is altered by applying a gate voltage, the conductivity of graphene can significantly change. Near the Dirac point, the resistivity of a graphene FET changes nonlinearly as a function of applied gate voltage. This nonlinearity has been used to achieve THz rectification in a graphene FET [47]. However, the heterodyne mixing of THz signals in a graphene based device has not been explored. Here, we will discuss the fabrication and measurement of graphene mixer in radio frequency, which serve as a platform for examining the design of a heterodyne graphene mixer for the THz band.

3.2 Methods

3.2.1 Design of The Graphene Mixer

A graphene FET mixer is designed to perform mixing in the microwave frequency range as a first step towards THz mixing on graphene. The design of the on chip RF components was carried out by our collaborators in the Smithsonian Astrophysical Observatory (SAO). As shown in Figure 3.1, the graphene FET mixer

consists of three components. They include a graphene FET at the center of the chip used for frequency mixing, a high pass filter designed for 30 GHz on the gate-source terminals to filter out the low frequency noise, and a bandstop filter to filter out the remaining RF and LO signal at the output port. The input of the mixer is a coplanar waveguide (CPW) with the band pass filter on the center connected to the gate of the graphene FET. It has a ground-signal-ground (GSG) configuration, so that we can use a high speed probe to feed in the signals. On the graphene FET, the graphene patch is attached to the ground on the two sides of the CPW. The drain is on the center, and it has a split gate to keep the structure symmetric. The drain of the FET is extended to the low pass filter on the output side, and the output IF signal is transmitted through the CPW.

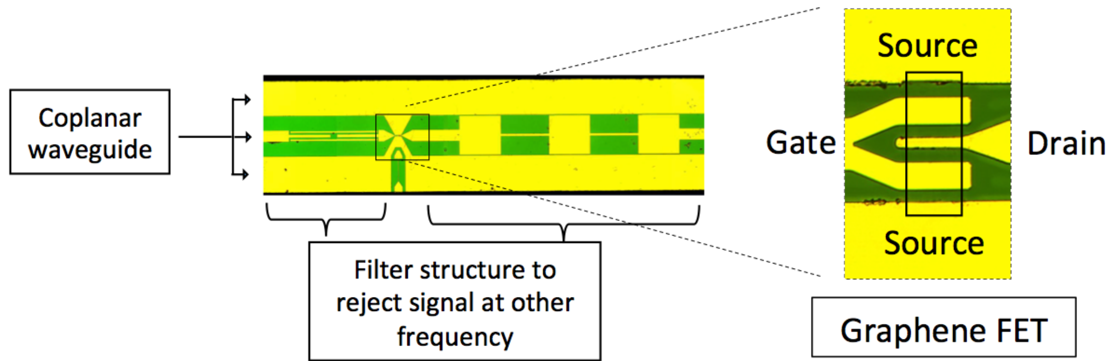

Figure 3.1: Optical micrograph of the graphene mixer with the graphene on the center

3.2.2 Device Fabrication

Large area CVD graphene was used to fabricate the graphene mixer. Single layer graphene was purchased from the Graphenea, and transferred to a 250um thick Si semi-insulating, high resistivity substrate. The Si substrate has 300 nm of thermal SiO_2 on the top to maximize the contrast for observing the graphene under an optical microscope [48]. The first step of the fabrication process was to pattern the graphene. For this, standard photoresist (AZ5214 IR) was spun on the sample at 3000 RPM for 30 seconds to produce a thickness of about 1.4 μm. Contact lithography was subsequently used to remove the photoresist where the graphene would be etched away by oxygen plasma. The next step was to use photoresist to pattern the source drain contacts lithographically, followed by metal deposition and lift-off. The metal contact is 200 nm thick Au on top of 10 nm thick Cr, where the Cr serves as an adhesion layer for the Au contact. After the source-drain contacts were formed on graphene, a 1-2 nm thick Al seed layer was deposited on graphene, and naturally oxidized to Al_2O_3 in ambient. This thin layer of Al_2O_3 was used as a seed layer for the subsequent oxide deposition to reduce the number of pinholes in the oxide [49]. The entire sample was then transferred to the reaction chamber of the atomic layer deposition (ALD) system for the gate oxide deposition. About 25 nm thick of ALD Al_2O_3 was deposited for the gate oxide, and the deposition temperature was 150 C°. After the oxide deposition, aligned lithography was used to define the pattern for the gate metal. It required precise alignment to avoid the overlap between gate metal and the source or drain metal. A 200 nm thick of Au

layer on top of 10 nm thick Cr was deposited and patterned for the gate contact. The dielectric layer was then removed at the location of the source and drain contacts by wet chemical etching, exposing the contact area for electrical connection such as wire bonding and test probes.

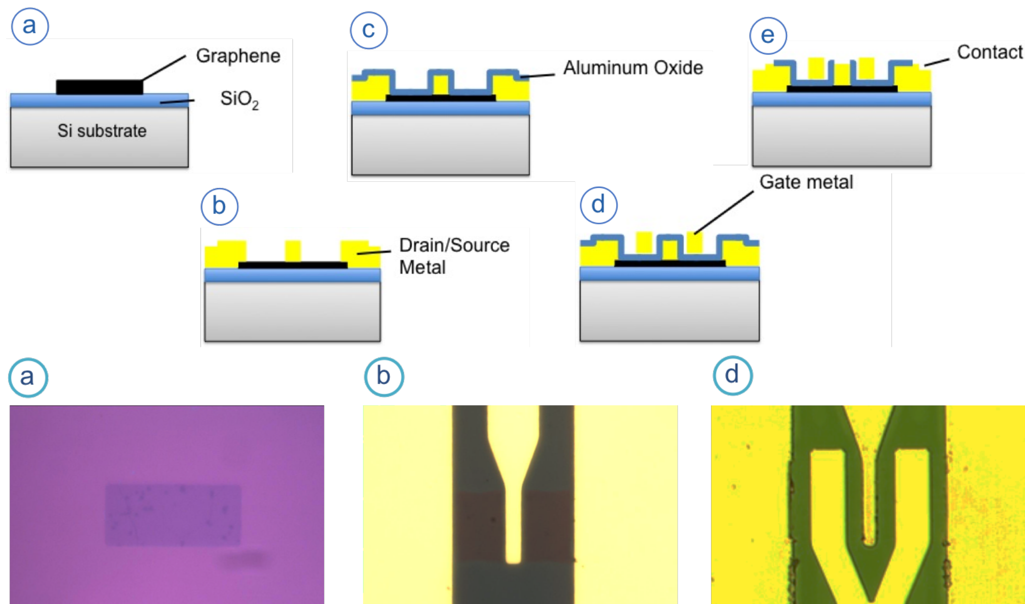

Figure 3.2: Device fabrication process for the graphene mixer in cross section and the corresponding micrographs. (a) Graphene patterning (b) Metal deposition for drain and source contacts (c) Al_2O_3 deposition by ALD (d) Gate metal deposition (e) Al_2O_3 etch for contact area

3.2.3 Experimental Setup

3.2.3.1 DC Characterization

Similar to the DC measurement setup from 2.2.2.1, the graphene FET mixer was connected to a set of two Keithley sourcemeters 2400 via needle probes. One of the sourcemeters was connected to the gate-source terminals to apply a gate voltage. The 25 nm gate oxide was observed to breakdown when the gate voltage

exceeds approximately 15 V. To avoid this, the gate voltage was swept from -12 V to 12 V, while monitoring the leakage current at the same time. The second sourcemeter was used to provide the source-drain bias during the gate sweep. The current was limited to 100 μA to avoid excessive Joule heating. The conductance of the device was measured as a function of applied gate voltage, thus the gate curves were obtained.

3.2.3.2 Frequency Mixing Measurement

We performed the RF mixing measurement by using the setup as described below. Two high speed RF signal generators were used as the sources of the RF signal and LO. The RF and LO sources were connected to a passive microwave combiner, and became a single input. A bias tee was connected in between the sources and the device to provide the connection for DC bias on the gate of the device. This allows the graphene FET mixer to be tuned to operate near the Dirac point, where the graphene mixer has the strongest nonlinear resistivity in response to gate voltage. The input line feeds in the signal and local oscillator through a high speed coplanar RF probe in GSG configuration. On the output side, the drain and source contacts were also connected to a similar coplanar probe in GSG configuration. A bias tee was used to connect a DC power supply and RF spectrum analyzer along with a external low pass filter. The DC power supply provides a DC bias on to source-drain terminals. On the other side, the low-pass filter removes the high frequency signal and LO that may leak from the input and preserves the

mixed IF signal. The spectrum analyzer measures the IF signal generated by the down frequency mixing from the graphene mixer.

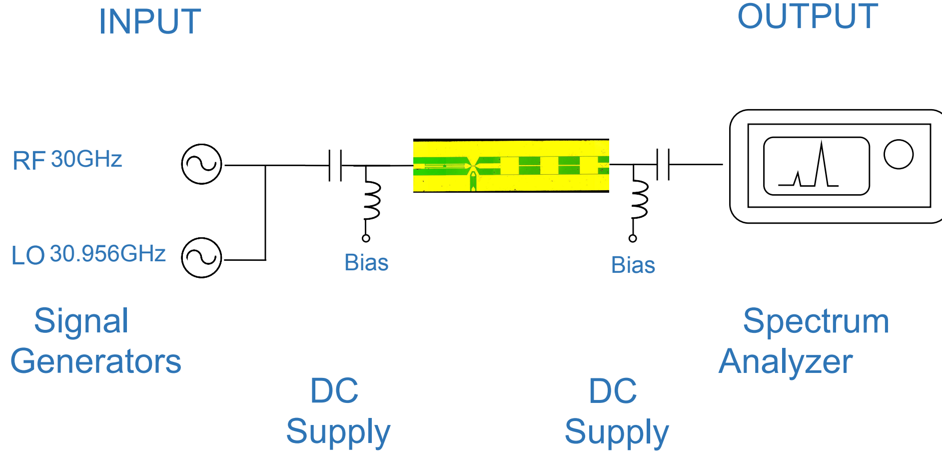

Figure 3.3: (a) Setup for the RF mixing measurement

3.2.3.3 Data Acquisition

The IF signal from the down frequency mixing was acquired by a spectrum analyzer (Keysight N9020A MXA Signal Analyzer). The center frequency was set to 956 MHz, with the frequency span of 5.1 kHz. For each set of the data taken in the measurement, the spectrum analyzer averaged the trace 10 times to reduce the background noise. To characterize the frequency dependence of our devices, we varied the frequency of the RF signal in the range from 16 GHz to 40 GHz. In all cases, the LO was tuned to 956 MHz below the RF frequency to maintain the IF at a constant frequency near 1 GHz. The power of the RF signal and LO were both 10 dBm unless otherwise specified. The drain bias was typically 0.01-0.5 V to keep the drain current below 100 μA and prevent excessive Joule heating. The applied gate voltage was held below 15 V to avoid the dielectric breakdown.

3.3 Results and Analysis

3.3.1 DC Characterization

The DC transport of the graphene FET inside the mixer was characterized by measuring its gating curve. The mixer has a dual gate design (See Figure 3.1), that runs two FETs in parallel. Two graphene FETs on the mixer were tested in parallel. The gating curve of the FETs were measured with the Keithley sourcementers. As expected, the measurements show that the resistance is a nonlinear function of the applied gate voltage. The resistance reached it maximum of about 830 Ω at the Dirac point when 2.5 V gate voltage was applied. The gate voltage ranged from -12 V to 12 V, and the current on/off ratio of the graphene FET was around 2. When measuring the gating curve of the graphene FET, we swept the gate voltage from the direction from negative to positive. We observed some hysteresis in the device response when we swept the gate voltage from the other direction. One of the reasons was that carriers can become trapped in between graphene and the SiO_2. The effect on conductance is in seconds time scale, and this is a rather slow process compared to the speed of the RF signal [50]. Once we found a stable point for the DC bias, the effect of the hysteresis is insignificant for the RF measurement because the frequency of the signal is much higher that the charge trapping process.

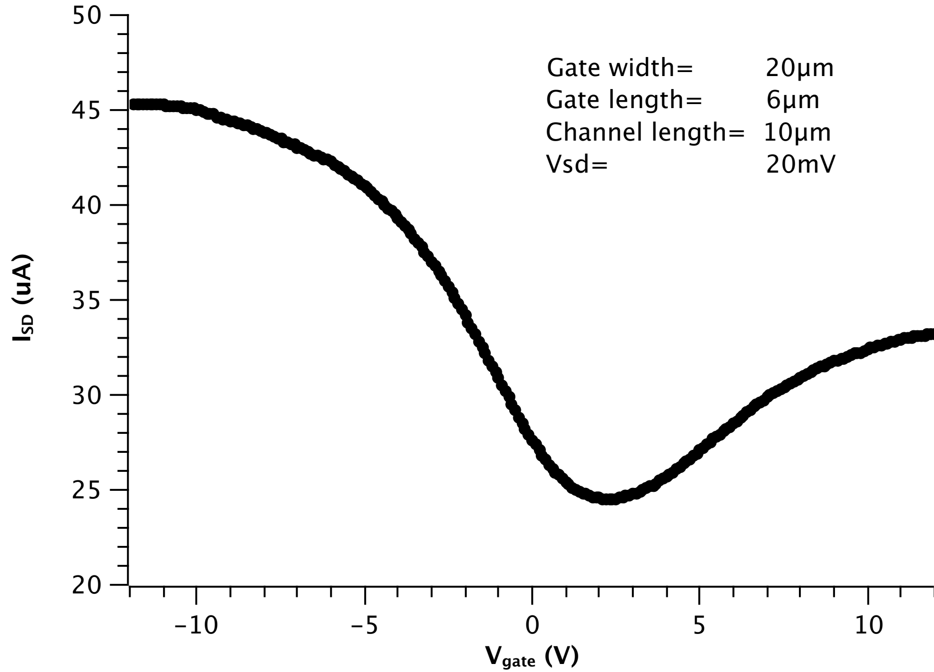

Figure 3.4: DC gating curve of the graphene FET

3.3.2 Frequency Dependence

The mixing performance of the graphene mixer as a function of frequency was observed by altering the frequency of the signals from the inputs. For the DC bias condition of the mixer, a DC gate voltage was applied on the graphene FET, such that the graphene mixer could operate near the Dirac point. The source-drain bias current was kept at 32 μA with a bias of 50 mV. The result of the output IF power as a function of the mixing frequency is shown in Figure 3.5. The output IF power lies between -66 dBm to -82 dBm. It reached its maximum downconversion power when operated at RF frequency of 30 GHz, where the mixer was designed to operate. We didn't observe any sharp cut-off within the range from 16 - 40 GHz. The fluctuation of the IF power over the range of the frequency may be caused by the frequency

response of the filter used for isolation. We note that the output power reported here is a lower estimate: the values plotted here were obtained directly from the reading of the spectrum analyzer, without taking into the account of the loss from the combiner, filter, cables, etc.

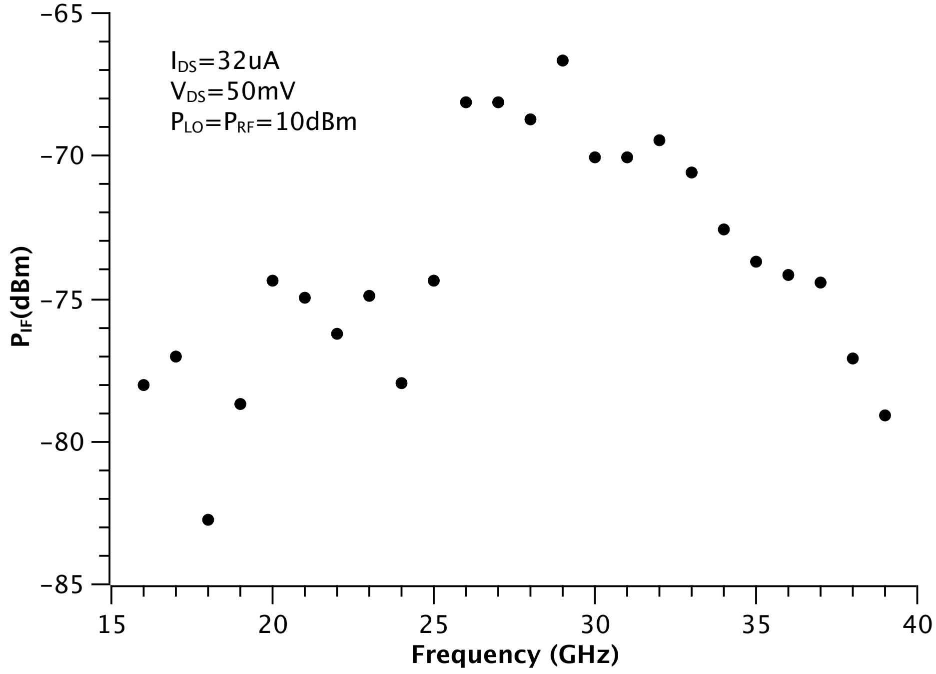

Figure 3.5: (a) Frequency mixing measurement of the graphene mixer. The IF output power is measured with RF and LO frequencies from 16-40 GHz

3.3.3 Power Dependence

To investigate the effect of the input power on mixing performance of the graphene mixer, we performed the power dependence measurement. The IF output power was measured, while changing the power level of the RF signal. The power of the RF signal was swept from -20 dBm to 10 dBm, while the LO power was fixed at 10 dBm. To avoid damaging the device, we kept the total power from the

inputs below 20 dBm. In this measurement, the frequency of the RF signal was 30.956 GHz, and the LO frequency is 30GHz. The difference of the RF and LO frequency was 956 MHz. The graphene mixer also had DC bias to operate around the Dirac point in order to obtain highest mixing efficiency. The gate voltage was set to around 7 V, where the resistivity of the graphene behave nonlinearly and can therefore be used for frequency mixing. The source-drain bias current was kept at 1.6 μA with the bias of 50 mV. The output signal at various input RF power was recorded by the spectrum analyzer, and the result is shown in Figure 3.7. As shown on the plot, the output RF power is linearly proportion to the input RF power. The conversion loss is between 66 dB to 69 dB, and the graphene FET mixer shows good linearity over a wide range of RF input power. For other existing graphene FET mixers, a conversion loss of between -30 to -40 dB in the 10 MHz range has been achieved [51]. A graphene mixer with low phase noise of -110 dBc/Hz operating in MHz range is also demonstrated by [52]. With nanostructure on the graphene in the channel of the FET, a subharmonic resistive mixer can achieve a conversion loss of 18 dB at 30 GHz [53].

3.3.4 Gate and Bias Dependence

The gate voltage and bias dependence of the mixer were examined, and the corresponding mixing performance was observed. For the gate voltage dependence measurement, the applied DC gate voltage varied from 0 - 7 V , and the IF output power was recorded at each voltage. The data was taken at the frequency of 30.956

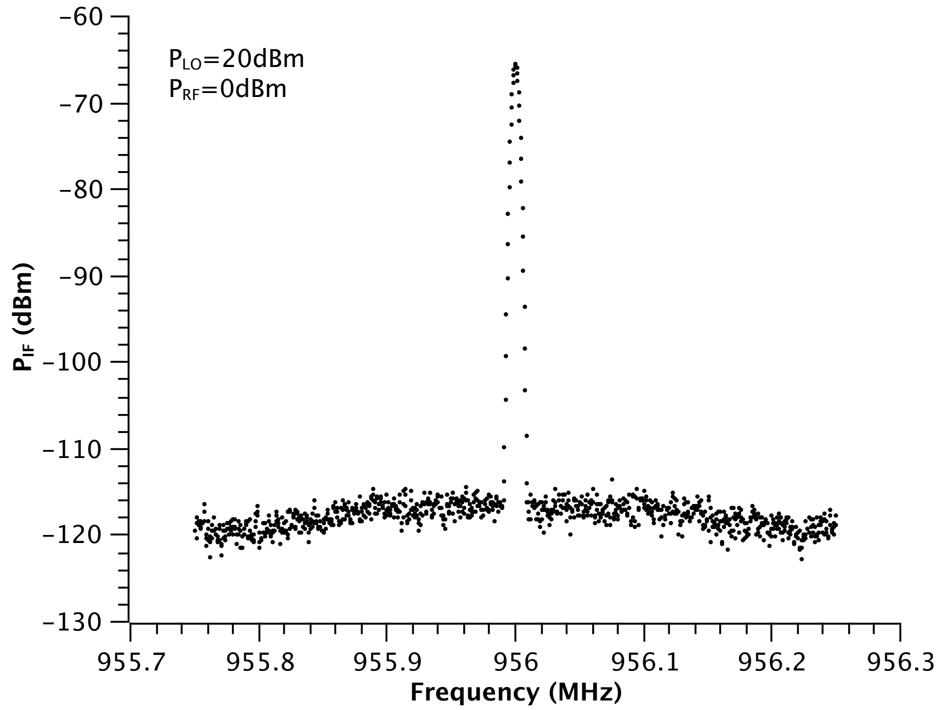

Figure 3.6: Output spectrum of the IF at 956 MHz. The corresponding RF and LO frequency are 30.956 GHz and 30 GHz.

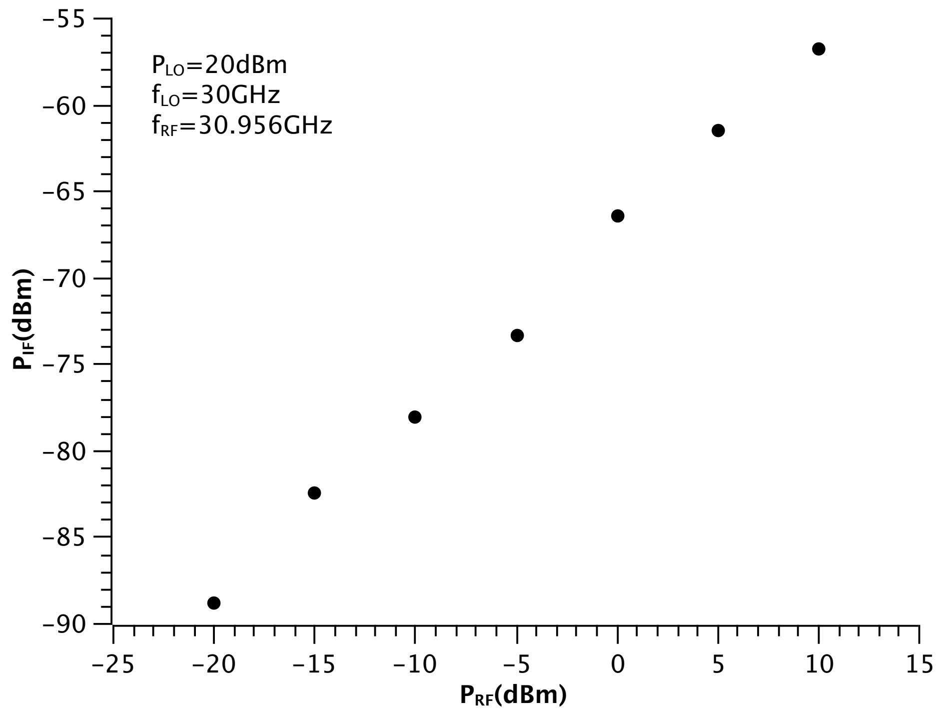

Figure 3.7: (a) Frequency mixing measurement for the graphene mixer as a function of input power. The RF power ranges from -20dbm-10dbm with 20dBm LO power. The measurement is done at the frequency of 30 GHz

GHz for RF and 30 GHz for LO , where the mixer gave the strongest output signal at the frequency. Both RF and LO had the input power of 10 dBm . The IF output was measured at 956 MHz with the spectrum analyzer for the downconversion mixing measurement. Figure 3.8 shows the result of the gate dependence measurement. The maximum output signal was found when the applied gate voltage was around 3.5 V and 6 V. This was because the nonlinearity of the resistance of the device was highest when it was very close to the Dirac point. When the mixer had the DC gate voltage adjusted to the Dirac point, the change of resistivity with respect to the gate voltage was at minimum . Therefore, the output signal significantly decreased. We note that the hysteresis was observed on the graphene mixer during the DC characterization. The gate voltage needed to bias the mixer at the Dirac point shifted slightly in each measurement. This effect was also observed in other graphene FET devices [50, 54]. One of the reason for this is the interface charges between the graphene and SiO_2, which get trapped at the interface, and take time to release when the gate voltage changes. For this reason, the voltage needed to reach the Dirac point shifted lightly over time during the measurements. For the bias dependence measurement, the IF output was measured with the gate voltage set close to the Dirac point to give maximum output. The strength of the IF signal only changed slightly with the change of source-drain bias. While the change of the response was stronger when the gate voltage (i.e. 0.5V) was further away from the Dirac point , the difference was less than 5dBm. The effect of the DC source-drain bias on the output signal power was relatively small.

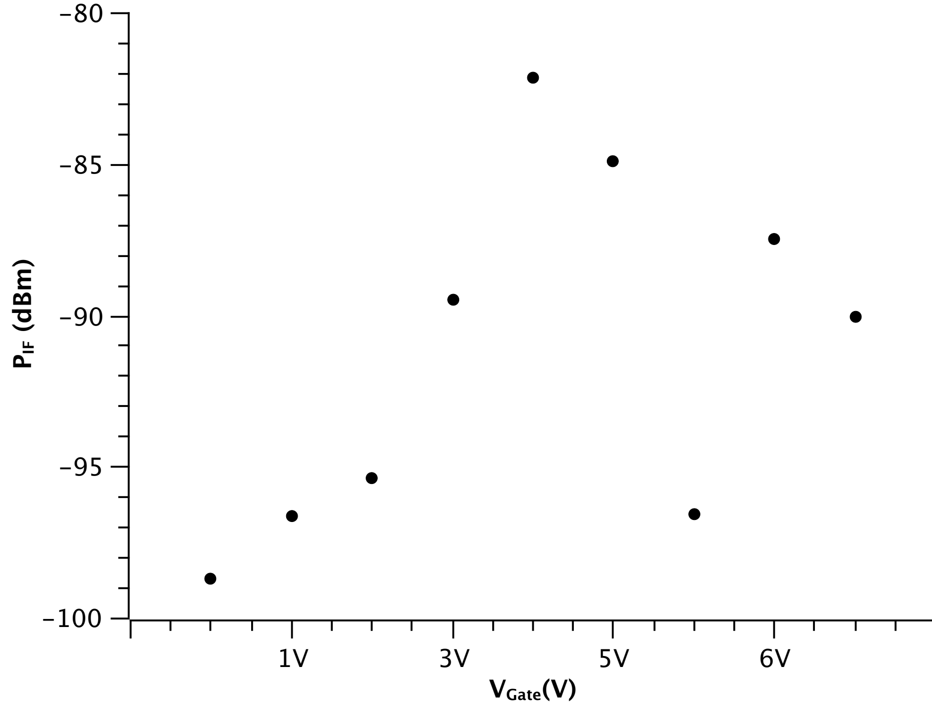

Figure 3.8: Frequency mixing measurement for the graphene mixer as a function of input power. The RF power ranges from -20 - 10 dbm with 20 dBm LO power. The measurement is done at the frequency of 30 GHz

3.4 Discussion and Future Work

The performance of the mixer can be further improved in several aspects, such as conversion efficiency and operating frequency range. This can be achieved by enhancing the nonlinearity, and lowering the RC constant for the high-speed application. For example, by using graphene with higher mobility (i.e. hydrogen intercalated graphene or hexagonal BN encapsulated graphene) provide a steeper gating curve in DC response. The steeper gating curve leads to stronge nonlinearity of the resistance, which should produce higher conversion efficiency for mixing. A more efficient electrostatic gating can also enhance the nonlinearity. This can be achieve by using gate dielectric which has higher permittivity, such as HfO_2. To

extend the frequency operation range of the mixer, a lower RC constant on the graphene FET is needed. The resistance of the mixer can be reduced by optimizing the resistance of the Ohmic contact. Edge-contacted on h-BN encapsulated graphene has been shown to have very low contact resistance, which could be incorporated to achieve a lower RC constant [55].

Ongoing effort has been put on the design of the antenna couple THz mixer based on graphene FET. While the design and the mixing measurement of the THz mixer will be done with our collaborators in the Smithsonian Astrophysics Observatory, the fabrication process will be developed here at UMD. For THz heterodyne mixing, a free space couple antenna can be integrated into the graphene mixer to efficiently collect the THz radiation for mixing. Our collaborators have been working on the design of a twin slot antenna for THz frequency. A twin slot antenna has symmetric radiation pattern with good efficiency, that makes it suitable for THz application. Additionally, microstrips couple to the drain and gate terminal can reduce the loss from the transmission of the output IF signal. Furthermore, a new device fabrication process is needed to build the THz mixer, mainly because of the size of the transistor need to be reduced to the nanoscale, such that the RC constant can be reduced for the THz application. It can be realized by incorporate nanofabrication process, such as e-beam lithography. On the other hand, a setup for the THz mixing measurement is needed to provide a platform to study the mixing behavior of graphene at THz frequency. In order to efficiently couple the THz radiation, it is important to minimize the interference on the Si substrate. Besides using the high resistivity Si substrate, a hemispherical Si lens can put on the back of the substrate

to focus the radiation and minimize the interference [56].The hemispherical Si lens can focus the radiation to back side of the device and couple to the antenna. Rather than losing the energy from the interference within the substrate, the hemispherical Si lens concentrates the energy on the device to yield larger output signal. Additionally, studying the mixing behavior at cryogenic temperature is also beneficial as graphene has ultrahigh mobility and steep gate curve at low temperature [25].

Chapter 4: Conclusion

In conclusion, two-dimensional materials have great potential for THz applications. In this thesis, we have used graphene and black phosphorus as examples to show that their unique material properties can be utilized for optoelectronics in THz region.

In chapter 2, we demonstrated the picosecond THz response of BP with antenna-coupled detector based on exfoliated BP flakes. The ultrafast rise time of about 20 ps is revealed in the time-resolved measurements. Also, a dominant photo-thermoelectric and a weaker bolometric effect are identified in the THz detection. The THz experiments also shown a strong in-plan anisotropy depending on the polarization, and is more pronounced than what we observed in NIR. From the Joule heating experiments, the intrinsic responsivity is estimated to be about 40 V/W, which is consistence with calculation of the THz absorption with using the free-carrier absorption model. Further optimization for the antenna impedance matching and enhancing the photo-thermoelectric effect are expected to result in responsivity beyond 40 V/W combined with the rise time of about 20 ps. That will make BP a superior candidate for future THz optoelectronics.

In chapter 3, frequency mixing with using the ambipolar transport character-

istic of graphene had been shown in the microwave regime. A frequency mixer based on graphene FET was fabricated and tested at RF frequencies to demonstrate the principle of operation for down frequency mixing. We also performed measurements for DC characterization to observe its nonlinear resistance in response to gate voltage, which was utilized for the frequency mixing. The mixer was further tested at the frequency from 16 GHz - 40 GHz to evaluate its mixing capability.

Bibliography

[1] Wikipedia, the free encyclopedia. Thz frequency in em spectrum, 2006. [Online; accessed Novermber 5, 2016].

[2] Xiaomu Wang, Aaron M Jones, Kyle L Seyler, Vy Tran, Yichen Jia, Huan Zhao, Han Wang, Li Yang, Xiaodong Xu, and Fengnian Xia. Highly anisotropic and robust excitons in monolayer black phosphorus. *Nature Nanotechnology*, 10(6):517–521, 2015.

[3] Andre K Geim and Konstantin S Novoselov. The rise of graphene. *Nature Materials*, 6(3):183–191, 2007.

[4] Heinrich Rubens and Benj W Snow. On the refraction of rays of great wavelength in rock-salt, sylvite, and fluorite. *The London, Edinburgh, and Dublin Philosophical Magazine and Journal of Science*, 35(212):35–45, 1893.

[5] Bradley Ferguson and Xi-Cheng Zhang. Materials for terahertz science and technology. *Nature Materials*, 1(1):26–33, 2002.

[6] Masayoshi Tonouchi. Cutting-edge terahertz technology. *Nature Photonics*, 1(2):97–105, 2007.

[7] Ruth M Woodward, Bryan E Cole, Vincent P Wallace, Richard J Pye, Donald D Arnone, Edmund H Linfield, and Michael Pepper. Terahertz pulse imaging in reflection geometry of human skin cancer and skin tissue. *Physics in Medicine and Biology*, 47(21):3853, 2002.

[8] Tadao Nagatsuma, Guillaume Ducournau, and Cyril C Renaud. Advances in terahertz communications accelerated by photonics. *Nature Photonics*, 10(6):371–379, 2016.

[9] Henry H Mantsch and Dieter Naumann. Terahertz spectroscopy: The renaissance of far infrared spectroscopy. *Journal of Molecular Structure*, 964(1):1–4, 2010.

[10] Calvin Yu, Shuting Fan, Yiwen Sun, and Emma Pickwell-MacPherson. The potential of terahertz imaging for cancer diagnosis: A review of investigations to date. *Quantitative Imaging in Medicine and Surgery*, 2(1):33–45, 2012.

[11] Mette Mogensen and Gregor BE Jemec. Diagnosis of nonmelanoma skin cancer/keratinocyte carcinoma: a review of diagnostic accuracy of nonmelanoma skin cancer diagnostic tests and technologies. *Dermatologic Surgery*, 33(10):1158–1174, 2007.

[12] AM Zolot, FR Giorgetta, E Baumann, JW Nicholson, WC Swann, I Coddington, and NR Newbury. Direct-comb molecular spectroscopy with accurate, resolved comb teeth over 43 THz. *Optics Letters*, 37(4):638–640, 2012.

[13] Yookyeong Carolyn Sim, Inhee Maeng, and Joo-Hiuk Son. Frequency-dependent characteristics of terahertz radiation on the enamel and dentin of human tooth. *Current Applied Physics*, 9(5):946–949, 2009.

[14] John F Federici, Brian Schulkin, Feng Huang, Dale Gary, Robert Barat, Filipe Oliveira, and David Zimdars. THz imaging and sensing for security applications-explosives, weapons and drugs. *Semiconductor Science and Technology*, 20(7):S266, 2005.

[15] Ian F Akyildiz, Josep Miquel Jornet, and Chong Han. Terahertz band: Next frontier for wireless communications. *Physical Communication*, 12:16–32, 2014.

[16] David H Auston, KP Cheung, JA Valdmanis, and DA Kleinman. Cherenkov radiation from femtosecond optical pulses in electro-optic media. *Physical Review Letters*, 53(16):1555, 1984.

[17] Ch Fattinger and D Grischkowsky. Terahertz beams. *Applied Physics Letters*, 54(6):490–492, 1989.

[18] Gerald Ramian. The new UCSB free-electron lasers. *Nuclear Instruments and Methods in Physics Research Section A: Accelerators, Spectrometers, Detectors and Associated Equipment*, 318(1):225–229, 1992.

[19] A Gover, A Faingersh, A Eliran, M Volshonok, H Kleinman, S Wolowelsky, Y Yakover, B Kapilevich, Y Lasser, Z Seidov, et al. Radiation measurements in the new tandem accelerator FEL. *Nuclear Instruments and Methods in Physics Research Section A: Accelerators, Spectrometers, Detectors and Associated Equipment*, 528(1):23–27, 2004.

[20] KW Berryman, ER Crosson, KN Ricci, and TI Smith. Coherent spontaneous radiation from highly bunched electron beams. *Nuclear Instruments and Methods in Physics Research Section A: Accelerators, Spectrometers, Detectors and Associated Equipment*, 375(1):526–529, 1996.

[21] VP Bolotin, NA Vinokurov, DA Kayran, BA Knyazev, EI Kolobanov, VV Kotenkov, VV Kubarev, GN Kulipanov, AN Matveenko, LE Medvedev, et al. Status of the Novosibirsk terahertz FEL. *Nuclear Instruments and Methods in Physics Research Section A: Accelerators, Spectrometers, Detectors and Associated Equipment*, 543(1):81–84, 2005.

[22] Armand Staprans, EarlW McCune, and Jack A Ruetz. High-power linear-beam tubes. *Proceedings of the IEEE*, 61(3):299–330, 1973.

[23] Jian Wei, David Olaya, Boris S Karasik, Sergey V Pereverzev, Andrei V Sergeev, and Michael E Gershenson. Sensitive hot-electron nanobolometers for terahertz astrophysics. *Nature Nanotechnology*, 3(8):496–500, 2008.

[24] KSA Novoselov, Andre K Geim, SVb Morozov, Da Jiang, MIc Katsnelson, IVa Grigorieva, SVb Dubonos, and AAb Firsov. Two-dimensional gas of massless

Dirac fermions in graphene. *Nature*, 438(7065):197–200, 2005.

[25] Kirill I Bolotin, KJ Sikes, Zd Jiang, M Klima, G Fudenberg, J Hone, Ph Kim, and HL Stormer. Ultrahigh electron mobility in suspended graphene. *Solid State Communications*, 146(9):351–355, 2008.

[26] Kin Fai Mak, Matthew Y Sfeir, Yang Wu, Chun Hung Lui, James A Misewich, and Tony F Heinz. Measurement of the optical conductivity of graphene. *Physical Review Letters*, 101(19):196405, 2008.

[27] Zhipei Sun, Tawfique Hasan, Felice Torrisi, Daniel Popa, Giulia Privitera, Fengqiu Wang, Francesco Bonaccorso, Denis M Basko, and Andrea C Ferrari. Graphene mode-locked ultrafast laser. *ACS Nano*, 4(2):803–810, 2010.

[28] Kostya S Novoselov, Andre K Geim, Sergei V Morozov, D Jiang, Y_ Zhang, Sergey V Dubonos, Irina V Grigorieva, and Alexandr A Firsov. Electric field effect in atomically thin carbon films. *Science*, 306(5696):666–669, 2004.

[29] Ying Ying Wang, Zhen Hua Ni, Ting Yu, Ze Xiang Shen, Hao Min Wang, Yi Hong Wu, Wei Chen, and Andrew Thye Shen Wee. Raman studies of monolayer graphene: the substrate effect. *The Journal of Physical Chemistry C*, 112(29):10637–10640, 2008.

[30] Vy Tran, Ryan Soklaski, Yufeng Liang, and Li Yang. Layer-controlled band gap and anisotropic excitons in few-layer black phosphorus. *Physical Review B*, 89(23):235319, 2014.

[31] Yukihiro Takao and Akira Morita. Electronic structure of black phosphorus: tight binding approach. *Physica B+ C*, 105(1-3):93–98, 1981.

[32] Likai Li, Yijun Yu, Guo Jun Ye, Qingqin Ge, Xuedong Ou, Hua Wu, Donglai Feng, Xian Hui Chen, and Yuanbo Zhang. Black phosphorus field-effect transistors. *Nature Nanotechnology*, 9(5):372–377, 2014.

[33] Alexander S Mayorov, Roman V Gorbachev, Sergey V Morozov, Liam Britnell, Rashid Jalil, Leonid A Ponomarenko, Peter Blake, Kostya S Novoselov, Kenji Watanabe, Takashi Taniguchi, et al. Micrometer-scale ballistic transport in encapsulated graphene at room temperature. *Nano Letters*, 11(6):2396–2399, 2011.

[34] Nathaniel M Gabor, Justin CW Song, Qiong Ma, Nityan L Nair, Thiti Taychatanapat, Kenji Watanabe, Takashi Taniguchi, Leonid S Levitov, and Pablo Jarillo-Herrero. Hot carrier–assisted intrinsic photoresponse in graphene. *Science*, 334(6056):648–652, 2011.

[35] Matt W Graham, Su-Fei Shi, Daniel C Ralph, Jiwoong Park, and Paul L McEuen. Photocurrent measurements of supercollision cooling in graphene. *Nature Physics*, 9(2):103–108, 2013.

[36] Fengnian Xia, Thomas Mueller, Roksana Golizadeh-Mojarad, Marcus Freitag, Yu-ming Lin, James Tsang, Vasili Perebeinos, and Phaedon Avouris. Photocurrent imaging and efficient photon detection in a graphene transistor. *Nano Letters*, 9(3):1039–1044, 2009.

[37] Xinghan Cai, Andrei B Sushkov, Ryan J Suess, Mohammad M Jadidi, Gregory S Jenkins, Luke O Nyakiti, Rachael L Myers-Ward, Shanshan Li, Jun Yan, D Kurt Gaskill, et al. Sensitive room-temperature terahertz detection via the photothermoelectric effect in graphene. *Nature Nanotechnology*, 9(10):814–819, 2014.

[38] Steven P Koenig, Rostislav A Doganov, Hennrik Schmidt, AH Castro Neto, and Barbaros Oezyilmaz. Electric field effect in ultrathin black phosphorus. *Applied Physics Letters*, 104(10):103106, 2014.

[39] Joshua D Wood, Spencer A Wells, Deep Jariwala, Kan-Sheng Chen, EunKyung Cho, Vinod K Sangwan, Xiaolong Liu, Lincoln J Lauhon, Tobin J Marks, and Mark C Hersam. Effective passivation of exfoliated black phosphorus transistors against ambient degradation. *Nano Letters*, 14(12):6964–6970, 2014.

[40] Jingsi Qiao, Xianghua Kong, Zhi-Xin Hu, Feng Yang, and Wei Ji. High-mobility transport anisotropy and linear dichroism in few-layer black phosphorus. *Nature Communications*, 5, 2014.

[41] Shanshan Li, Gagan Kumar, and Thomas E Murphy. Terahertz nonlinear conduction and absorption saturation in silicon waveguides. *Optica*, 2(6):553–557, 2015.

[42] Martin Mittendorff, Stephan Winnerl, Josef Kamann, Jonathan Eroms, Dieter Weiss, Harald Schneider, and Manfred Helm. Ultrafast graphene-based broadband THz detector. *Applied Physics Letters*, 103(2):021113, 2013.

[43] Martin Mittendorff, Josef Kamann, Jonathan Eroms, Dieter Weiss, Christoph Drexler, Sergey D Ganichev, Jochen Kerbusch, Artur Erbe, Ryan J Suess, Thomas E Murphy, et al. Universal ultrafast detector for short optical pulses based on graphene. *Optics Express*, 23(22):28728–28735, 2015.

[44] Yue Liu, Tony Low, and P Paul Ruden. Mobility anisotropy in monolayer black phosphorus due to scattering by charged impurities. *Physical Review B*, 93(16):165402, 2016.

[45] Ryan J Suess, Mohammad M Jadidi, Thomas E Murphy, and Martin Mittendorff. Carrier dynamics and transient photobleaching in thin layers of black phosphorus. *Applied Physics Letters*, 107(8):081103, 2015.

[46] Ryan J Suess, Edward Leong, Thomas E Murphy, and Martin Mittendorff. Intrinsic Speed of a Black Phosphorus Photoconductive Detector. In *CLEO: QELS_Fundamental Science*, pages JW2A–41. Optical Society of America, 2016.

[47] L Vicarelli, MS Vitiello, D Coquillat, A Lombardo, AC Ferrari, W Knap, M Polini, V Pellegrini, and A Tredicucci. Graphene field-effect transistors as room-temperature terahertz detectors. *Nature Materials*, 11(10):865–871, 2012.

[48] P Blake, EW Hill, AH Castro Neto, KS Novoselov, D Jiang, R Yang, TJ Booth, and AK Geim. Making graphene visible. *Applied Physics Letters*, 91(6):063124, 2007.

[49] Seyoung Kim, Junghyo Nah, Insun Jo, Davood Shahrjerdi, Luigi Colombo, Zhen Yao, Emanuel Tutuc, and Sanjay K Banerjee. Realization of a high mobility dual-gated graphene field effect transistor with Al_2O_3 dielectric. *ArXiv Preprint arXiv:0901.2901*, 2009.

[50] Haomin Wang, Yihong Wu, Chunxiao Cong, Jingzhi Shang, and Ting Yu. Hysteresis of electronic transport in graphene transistors. *ACS Nano*, 4(12):7221–7228, 2010.

[51] Han Wang, Allen Hsu, Justin Wu, Jing Kong, and Tomas Palacios. Graphene-based ambipolar RF mixers. 2010.

[52] JS Moon, D Curtis, D Zehnder, S Kim, DK Gaskill, GG Jernigan, RL Myers-Ward, CR Eddy, PM Campbell, K-M Lee, et al. Low-phase-noise graphene FETs in ambipolar RF applications. *IEEE Electron Device Letters*, 32(3):270–272, 2011.

[53] Omid Habibpour, Josip Vukusic, and Jan Stake. A 30-GHz integrated subharmonic mixer based on a multichannel graphene FET. *IEEE Transactions on Microwave Theory and Techniques*, 61(2):841–847, 2013.

[54] Gopinadhan Kalon, Young Jun Shin, Viet Giang Truong, Alan Kalitsov, and Hyunsoo Yang. The role of charge traps in inducing hysteresis: capacitance–voltage measurements on top gated bilayer graphene. *Applied Physics Letters*, 99(8):083109, 2011.

[55] L Wang, I Meric, PY Huang, Q Gao, Y Gao, H Tran, T Taniguchi, K Watanabe, LM Campos, DA Muller, et al. One-dimensional electrical contact to a two-dimensional material. *Science*, 342(6158):614–617, 2013.

[56] Daniel F Filipovic, Steven S Gearhart, and Gabriel M Rebeiz. Double-slot antennas on extended hemispherical and elliptical silicon dielectric lenses. *IEEE Transactions on Microwave Theory and Techniques*, 41(10):1738–1749, 1993.